



Article

On the Mechanism of Magnesium Storage in Micro- and Nano-Particulate Tin Battery Electrodes

Francisco Nacimiento, Marta Cabello, Carlos Pérez-Vicente, Ricardo Alcántara , Pedro Lavela , Gregorio F. Ortiz * and José L. Tirado

Departamento de Química Inorgánica e Ingeniería Química, Instituto Universitario de Investigación en Química Fina y Nanoquímica IUIQFN, Universidad de Córdoba, Campus de Rabanales, Edificio Marie Curie, E-14071 Córdoba, Spain; q92nacof@uco.es (F.N.); z22cabbm@uco.es (M.C.); iq3pevic@uco.es (C.P.-V.); iq2alror@uco.es (R.A.); iq1lacap@uco.es (P.L.); iq1ticoj@uco.es (J.L.T.)

* Correspondence: q72maorg@uco.es; Tel.: +34-957-218637

Received: 8 June 2018; Accepted: 4 July 2018; Published: 6 July 2018



Abstract: This study reports on the electrochemical alloying-dealloying properties of Mg_2Sn intermetallic compounds. ^{119}Sn Mössbauer spectra of β -Sn powder, thermally alloyed cubic- Mg_2Sn , and an intermediate $MgSn$ nominal composition are used as references. The discharge of a Mg/micro-Sn half-cell led to significant changes in the spectra line shape, which is explained by a multiphase mechanism involving the coexistence of c- Mg_2Sn , distorted $Mg_{2-\delta}Sn$, and Mg-doped β -Sn. Capacities and capacity retention were improved by using nanoparticulate tin electrodes. This material reduces significantly the diffusion lengths for magnesium and contains surface SnO and SnO_2 , which are partially electroactive. The half-cell potentials were suitable to be combined versus the $MgMn_2O_4$ cathodes. Energy density and cycling properties of the resulting full Mg-ion cells are also scrutinized.

Keywords: electrode nanomaterials; magnesium-tin intermetallics; magnesium-ion batteries; Sn-119 Mössbauer spectroscopy

1. Introduction

Recent concerns regarding the future availability of lithium (Li) [1–4], together with safety issues [5] affecting Li-ion batteries have prompted expanding research activity on alternatives to lithium. Due to its high abundance, easy extraction and moderate cost, magnesium (Mg) is one of the multivalent elements that show promising possibilities [6–13]. Despite its lower potential compared with lithium, Mg electrodes provide higher volumetric capacity and shows a better reconstruction of its surface on cycling, being less prone to form dendrites on electroplating. Mg^{2+} ions have a similar radius to Li^+ ones and avoid pronounced volume changes on cycling. However, there is a major difficulty in obtaining reliable Mg-anode batteries, related with the stability of electrolyte solutions [12,13]. Thus, electrolytes commonly stable versus Mg are mostly unstable versus common cathodes found so far and vice versa. For this reason, the research for alternative anodes and hence the concept of Mg-ion batteries is also valid for this alkali-earth element. Recently, the chemical and electrochemical Mg deinsertion from $MgMn_2O_4$, which leads to $Mg_{1-x}Mn_2O_4$ or λ - MnO_2 , has been reported using both aqueous and non-aqueous electrolytes [14–16]. While examining the possible use of several materials as anodes to be combined vs. $MgMn_2O_4$ as a positive electrode, the most successful results were found for tin (Sn), a material previously reported to have reversible electrochemical alloying reactions with Mg [17]. To study these alloying reactions, we apply ^{119}Sn Mossbauer spectroscopy (MS), a uniquely selective technique, to study changes in the oxidation state and chemical environment of tin. When tin oxides and intermetallic compounds are used as active electrode material in lithium

batteries, ^{119}Sn MS provides valuable information [18–22]. Particularly, Aldon et al. found ^{119}Sn MS useful to study lithium insertion in c- Mg_2Sn [21].

A ^{119}Sn Mössbauer study is reported here for Sn powdered electrodes in Mg test cells, to unveil the details of the complex mechanism of the electrochemical reaction, which involves a tin-rich intermetallic phase with an electric field gradient environment of tin atoms and cubic Mg_2Sn . Also, due to the increasing interest in nanomaterials for battery applications [23,24], the optimization of the electrode was carried out by using a nano-dispersed Sn- SnO_x composite powder that provides a unique surface electroactive coating of tin oxides, allowing for better cycling stabilities. Finally, the nano-tin electrodes are combined with a low temperature MgMn_2O_4 material recently reported by our research group to obtain a novel suitable Mg-ion battery.

2. Materials and Methods

Commercial magnesium strip (purity $\geq 99\%$, Sigma-Aldrich Química S.L., Madrid, Spain) and micro- and nano-Sn (Aldrich) powders were used as received. Thermally prepared Mg-Sn intermetallic samples included stoichiometric crystalline Mg_2Sn and a sample with MgSn nominal stoichiometry. Both thermal samples were obtained from mechanical mixtures of Mg and micro-Sn, which were heated at $700\text{ }^\circ\text{C}$ for 1 h and then cooled to room temperature at $4\text{ }^\circ\text{C min}^{-1}$ in a N_2 atmosphere. The low-temperature spinel (LT)- MgMn_2O_4 was prepared as described elsewhere [16], following the Pechini method. The dry powdered precursor was first heated at $200\text{ }^\circ\text{C}$, ground in an agate mortar and then heated at $400\text{ }^\circ\text{C}$ for ten hours.

The electrochemical experiments were performed in a multichannel VMP instrument (Bio-Logic, Barcelona, Spain). Swagelok-type cells were mounted in an M-Braun glove-box filled with Ar. Tin powders and magnesium strips were used as received. The working electrodes were a mixture of active material:carbon black:polyvinylidene difluoride (PVDF) binder in a 80:10:10 ratio supported on Ti substrate. The carbon black additive was supplied by Société des Accumulateurs Fixes et de Traction (S.A.F.T., Bordeaux, France). The electrode mass load was $3.0\text{--}5.0\text{ mg cm}^{-2}$. Several non-aqueous electrolyte solutions were tested, including 0.5 M PhMgCl in tetrahydrofuran (THF) or 0.5 M EtMgCl in THF for Mg/Sn half cells, and $0.5\text{ M Mg}(\text{ClO}_4)_2$ in acetonitrile (AN) for full cells. Mg-ion full cells were tested in SwagelokTM-type three-electrode cells to monitor separately cathode and anode voltages versus a reference electrode consisting of a metallic Mg disk.

X-ray diffraction (XRD) measurements were carried out in a Bruker D8-Advance instrument (Bruker Española S.A., Madrid, Spain) with $\text{CuK}_{\alpha 1}$ radiation. Ex-situ XRD patterns of discharged electrodes were recorded by dismantling the electrochemical cells in the dry box under Ar atmosphere and, after recovering the electrodes and separating them from the Ti collector, covering them with a Kapton bag to avoid contact with air.

The ^{119}Sn Mössbauer spectra (MS) were recorded in a WissEl instrument (WissEl-Wissenschaftliche Elektronik GmbH, Starnberg, Germany) at room temperature. The spectra were recorded with adequate acquisition time to permit a deconvolution, typically ten days. The ^{119}Sn isomer shifts are referenced to BaSnO_3 . A pure $\beta\text{-Sn}$ foil was used for the calibration. For the fitting of the experimental spectra, the WINSO1.0 program (F. Landry, P. Schaaf, WinISO: Windows Mössbauer Fitting Program, unpublished), Lorentzian line-shape absorption peaks, and a least-squares method were employed. When the fitting process reached the convergence, the quality of the fitting was controlled by the classical χ^2 -test. The Mössbauer spectra of discharged electrodes were recorded ex-situ by putting the active material under Ar atmosphere in polybags (Aldrich), which were hermetically closed by heat-sealing with a commercial heat sealer at $150\text{ }^\circ\text{C}$.

Field-Emission Scanning Electron Microscope (FESEM) images were obtained in JEOL FESEM (Izasa Scientific, Madrid, Spain) 1400 provided with Energy-dispersive X-ray spectroscopy (EDX).

3. Results

Figure 1 shows the X-ray diffraction patterns of thermally prepared, crystalline cubic c-Mg₂Sn, a fluorite-type structure, and the thermally prepared MgSn material, which contains both crystalline β -Sn and c-Mg₂Sn with visible traces of MgO impurities and unreacted Mg.

Figure 2a shows the ¹¹⁹Sn MS data for the commercial tin microparticles. The observed isomer shift (IS) value of 2.561₉ mm s⁻¹ (Table 1) and its negligible quadrupolar splitting are consistent with a high-purity and well crystallized β -Sn phase.

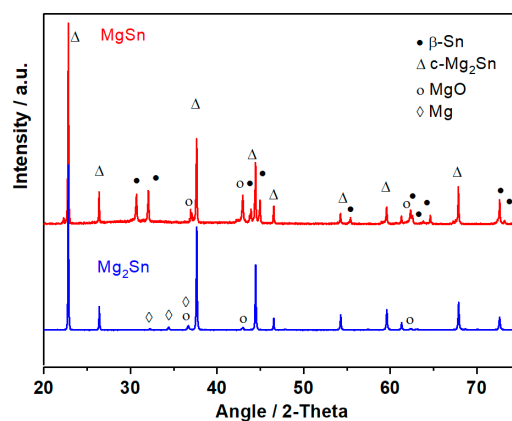


Figure 1. Powder X-ray diffraction (XRD) patterns of the thermally prepared samples with Mg₂Sn and MgSn nominal compositions.

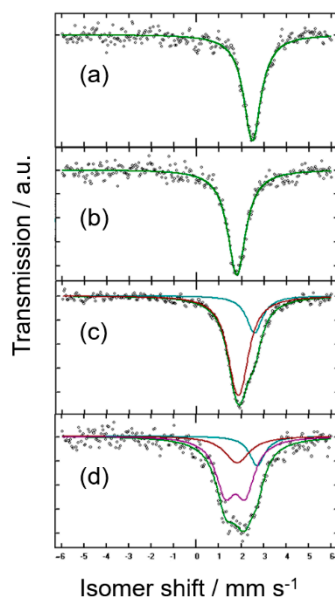


Figure 2. ¹¹⁹Sn Mössbauer spectra of (a) tin microparticles, and thermally prepared samples with (b) Mg₂Sn and (c) MgSn nominal compositions. (d) micro-Sn electrode after discharge in Mg half-cell to a Mg_{0.4}Sn nominal composition.

Figure 2b shows the spectrum of the crystalline Mg₂Sn alloy. The IS value of 1.847₉ mm s⁻¹ is ascribable to cubic c-Mg₂Sn [21,25]. In agreement with the well-known fluorite-type structure of c-Mg₂Sn, tin atoms are eight-fold coordinated by magnesium and twelve-fold coordinated by tin second neighbors, which is in contrast with the use of less and more directional covalent bonds in β -Sn and agrees with the significantly lower isomer shift relative to β -Sn (Figure 2a). Again, the highly symmetric coordination of tin atoms in the structure impedes a quadrupole splitting of the signal

(Table 1). The spectrum of thermal MgSn shows two deconvoluted contributions close to c-Mg₂Sn and β-Sn-related phases (Figure 2c). However, this spectrum reveals unexpected results. Thus, the singlets ascribable to crystalline β-Sn and c-Mg₂Sn were not sufficient to fit the spectrum. A significant quadrupole splitting (0.30₄ mm s⁻¹) of the low IS signal was also present (Table 1). This visually unresolved doublet is indicative of the presence of tin nuclei in a low symmetry environment of Sn atoms. It is probably due to incomplete coordination by Mg atoms, in a metastable, non-stoichiometric and distorted d-Mg_δSn phase, which is not discerned from the crystalline products in the XRD patterns. This result is consistent with the report by Sirkin et al. [26] on quenched ternary Sn-Mg-M alloys, and latter corroborated by theoretical calculations by Fries and Lukas [27].

Table 1. Isomer shift (IS), quadrupolar splitting (QS), line width (LW), % contribution and attribution of the signals appearing in the ¹¹⁹Sn Mössbauer spectra of commercial micro- and nano-Sn, mechanochemically produced Mg₂Sn, and discharged/recharged electrodes. * Recoilless fractions, *f* = 0.05 (Sn). Reproduced with permission of [28,29]. Copyright Elsevier, 2000, 1966. *f* = 0.3 (c-Mg₂Sn) Reproduced with permission of [29]. Copyright Elsevier, 1966. *f* = 0.15 (Mg_{2-δ}Sn; ca. half of the reported value [29], due to the possible tin excess). These values were used to convert spectral contributions (%) into semiquantitative composition (%_{corr}).

Sample (Nominal)	IS/mms ⁻¹	QS/mms ⁻¹	LW/mms ⁻¹	%	% _{corr} *	Attribution
(a) micro-Sn	2.561 ₉	-	0.95 ₃	100	100	β-Sn
(b) thermal-Mg ₂ Sn	1.847 ₉	-	0.99 ₃	100	100	c-Mg ₂ Sn
(c) thermal-MgSn	2.64 ₃	-	0.87 ₇	24	49	β-Sn
	1.91 ₃	0.30 ₄	0.96 ₄	76	51	Mg _{2-δ} Sn
(d) micro-Mg _{0.4} Sn	2.79 ₈	-	1.83 ₁	15	38	β-Sn
discharged	1.8 ₂	-	1.4 ₅	21	9	c-Mg ₂ Sn
	1.79 ₅	0.908 ₂	1.051 ₂	64	53	Mg _{2-δ} Sn

Figure 3a,b shows the cycling properties of the Mg/0.5 M PhMgCl (THF)/micro-Sn cell. Extremely low capacity values were obtained in the 0.01–0.6 V potential window, although the capacity increases upon cycling (<10 mA h g⁻¹), probably indicating the progressive conditioning of the metal electrode surface. According to the Gibbs phase rule, the presence of well-defined plateaus in both discharge and charge should be consistent with a biphasic mechanism of the alloying-dealloying reaction:



The reaction mechanism of the micro-Sn electrodes was explored by using ¹¹⁹Sn MS. Figure 2d shows the results for a discharged electrode prepared by applying multiple galvanostatic pulses followed by relaxation periods to a Mg/micro-Sn half-cell until a stable nominal Mg_{0.4}Sn stoichiometry was achieved. The spectrum shows significant changes in line shape as referred to the pristine tin microparticles (see Figure 2a) that agree with tin electroactivity. The IS parameters shown in Table 1 evidence the simultaneous presence of a Mg-deficient, distorted Mg_{2-δ}Sn phase, a β-Sn-related phase with possible Mg doping and c-Mg₂Sn, which partially agrees with the biphasic mechanism suggested above. The low proportion of c-Mg₂Sn is indicative of impediments to the full conversion of the tin microparticles, probably due to an incomplete diffusion of magnesium through the larger tin particles. Moreover, the high broadening and significant quadrupole splitting of the d-Mg_δSn signal may point to a structural deterioration and/or partial Mg alloying in a metastable phase yielding many different local environments of the tin atoms. It is well known that electrochemical reactions may lead to metastable products, thus being one of the most useful soft-chemistry synthetic routes for the solid state [18–22].

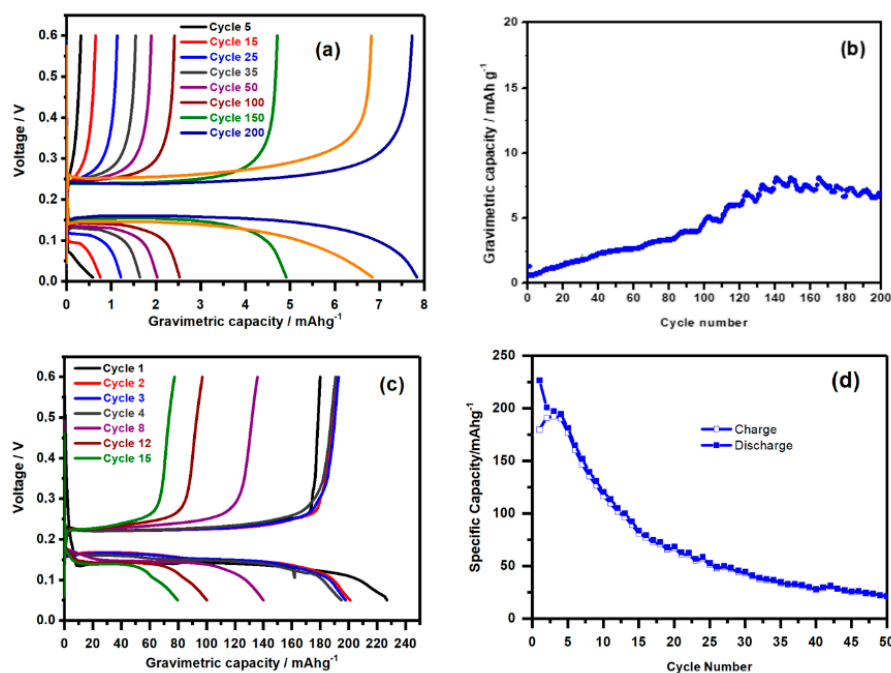


Figure 3. (a) Galvanostatic charge-discharge plots and (b) cycling performance at at 10 mA/g (C/20) current density of microparticulate β -Sn in Mg half-cell, using 0.5 M PhMgCl in THF as electrolyte. (c) Galvanostatic charge-discharge plots and (d) cycling performance at 10 mA/g (C/20) of nanoparticulate-Sn in in Mg half-cell using 0.5 M EtMgCl in THF as electrolyte.

Table 2. IS, QS, LW, % contribution and attribution of the signals appearing in the ^{119}Sn Mössbauer spectra of commercial micro- and nano-Sn, mechanochemically produced Mg_2Sn and discharged/recharged electrodes. * Recoilless fractions, $f = 0.05$ (Sn and d- Mg_5Sn), 0.35 (SnO), 0.60 (SnO_2), and 0.3 (c- Mg_2Sn) [28,29]. Copyright Elsevier, 2000, 1966. These values were used to convert spectral contributions (%) into semiquantitative composition (%_{corr}).

Sample (Nominal)	IS/mms ⁻¹	QS/mms ⁻¹	LW/mms ⁻¹	%	% _{corr} *	Attribution
(a) nano-Sn	2.579 ₈	-	1.41 ₉	33	76	β -Sn
	2.75 ₃	1.52 ₅	1.12 ₂	25	2	SnO
	0.026 ₇	1.58 ₁	1.16 ₅	42	13	SnO ₂
(b) nano- $\text{Mg}_{1.3}\text{Sn}$ discharged	1.87 ₁	-	0.88 ₄	40	50	c- Mg_2Sn
	2.85 ₆	0.90 ₆	1.0 ₁	27	29	SnO
	0.05 ₂	0.53 ₃	0.83 ₆	33	21	SnO ₂
(c) thermal- MgSn discharged + charged	2.67 ₂	-	1.04 ₃	14	60	d- Mg_5Sn
	1.90 ₃	-	1.04 ₄	9	7	c- Mg_2Sn
	2.81 ₂	1.22 ₃	1.04 ₁	23	14	SnO
	0.05 ₁	0.55 ₁	0.94 ₂	54	19	SnO ₂
(d) micro- $\text{Mg}_{0.4}\text{Sn}$ discharged + fully charged	2.70 ₈	-	0.87 ₄	15	60	d- Mg_5Sn
	2.71 ₂	1.57 ₃	0.87 ₇	26	17	SnO
	0.05 ₁	0.54 ₂	0.96 ₃	61	23	SnO ₂

To improve the electrochemical performance, a nanodispersed commercial sample (nano-Sn) was also assessed. ^{119}Sn MS data were also recorded. This spectrum was deconvoluted in several components attributed to β -Sn, a quadrupole split signal of SnO (IS = 2.65 mm s⁻¹), and SnO₂ with a cassiterite structure with IS ca. 0.0 mm s⁻¹ (Figure 4a and Table 2) [28]. The high intensity of the signals attributed to tin oxides, as compared with that of metallic tin is a consequence of the significantly lower f value for the latter. The necessary corrections lead to an atomic percentage of 76% β -Sn. The XRD pattern shows reflections of β -Sn and some additional low intensity lines that could be ascribable

to SnO (Figure 5) to support this conclusion. The presence of the oxides may involve the surface oxidation of the tin nanoparticles. This process is particularly visible in nanoparticulate materials due to their high surface-to-volume ratio. However, its presence could provide passivation of the electrode material that could prevent undesirable surface reactions with the electrolyte during the cycling or contribute to the total capacity if the oxides are electroactive. Figure 6 shows the FESEM images of micro and nano-Sn. In contrast to the ca. 100 μm particles of crystalline tin, nano-Sn shows particles around 100 nm. Also, the EDX spectra showed an average Sn/O atomic ratio of 1.16, and the composition mapping showed a uniform distribution of oxygen in the surface of the particles. With this in mind, we decided to use the nano-Sn sample without further chemical treatments for the electrochemical experiments.

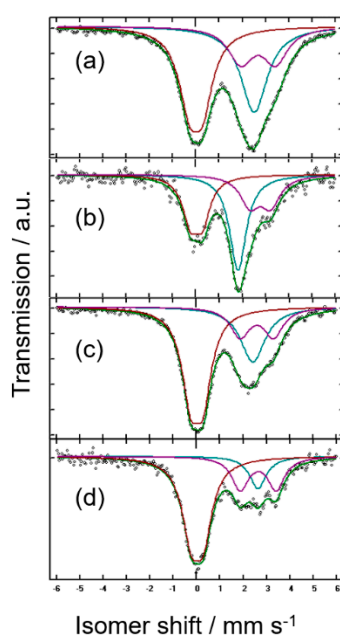


Figure 4. ^{119}Sn Mössbauer spectra of (a) Commercial nano-Sn, and (b) discharged nano-Sn electrodes in Mg half-cell to a $\text{Mg}_{1.3}\text{Sn}$ nominal composition. (c) Discharged-charged nano-Sn electrodes in Mg half-cell to a $\text{Mg}_{0.4}\text{Sn}$ nominal composition. (d) Discharged-fully charged nano-Sn electrodes in Mg half-cell.

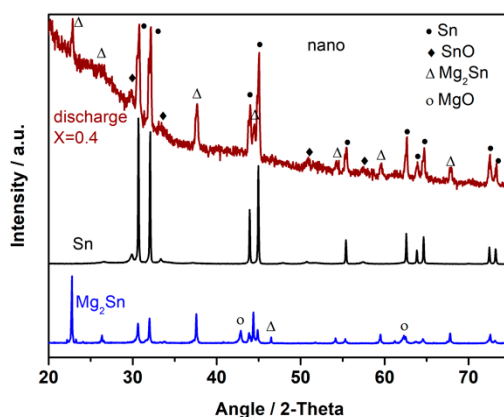


Figure 5. XRD pattern of commercial nano-Sn, and discharged nano-Sn electrode in Mg half-cell at Mg_xSn nominal compositions with $x = 0.4$ and $x = 2.0$.

Figure 3c,d shows the galvanostatic cycling experiments of Mg/nano-Sn half-cells. The initial capacity (225 mA h g^{-1}) is higher and cell polarization is lower than that of micro-Sn cell,

preserving well-defined plateaus. However, capacity fades for prolonged cycling, as that of micro-Sn, probably because of the poor response of the Mg metal electrode in the used electrolytes. However, nanodispersion is expected to be a suitable strategy to improve the initial capacity of full Mg-ion batteries, such as the proof of concept discussed below. The average discharge and charge voltages are 0.1 V and 0.25 V, respectively. The limited cell polarization and low charge potential suggest that a Sn/0.5 M PhMgCl (THF)/MgMn₂O₄ full cell (ca. 2.0 V) would provide a suitable energy density.

Figure 4b shows ¹¹⁹Sn MS data for nano-Sn electrodes after discharge to a nominal Mg_{1.3}Sn composition. The fitting parameters in Table 2 reveal the expected formation of c-Mg₂Sn; however, the tin oxides initially present in the samples are still present, thus offering a sufficient coating of the tin nanoparticles to be preserved during the alloying-dealloying process and stabilize the electrode structure upon cycling. The XRD pattern for *x* = 0.4 in Figure 5 is also in agreement with the MS data. The good reversibility of the process is exemplified by the ¹¹⁹Sn MS data for nano-Sn electrodes after recharge to a nominal Mg_{0.4}Sn composition (Figure 4c,d and Table 2). Although the oxide lines were always present, it can be highlighted that the initial SnO₂/SnO ratio in nano-Sn decreases during the discharge and increases again during charge. The SnO₂/SnO pair can be then considered electroactive, as shown in other systems [28]. Not only does this prevent undesirable surface reactions but it also contributes to the overall capacity.

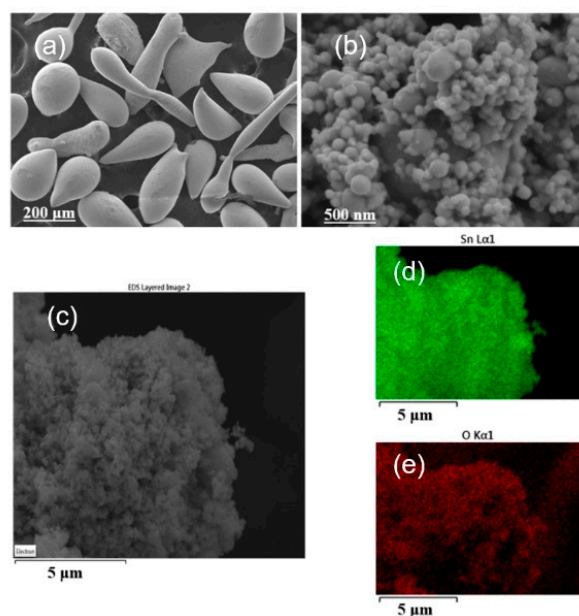


Figure 6. FESEM (Field-Emission Scanning Electron Microscope) images of (a) micro-Sn, and (b,c) nano-Sn. EDX composition mapping of nano-Sn: (d) tin and (e) oxygen.

A better perspective of the possible use of these materials as anodes in Mg-ion batteries can be given by trying their electrochemical behavior in full cells. For this purpose, the cycling properties of the nano-Sn/MgMn₂O₄ full cells were tested with different electrolyte solutions. The expected overall reaction can be written as:



Due to the incompatibility of the organometallic electrolytes versus MgMn₂O₄ [16], and perchlorate electrolytes in acetonitrile versus Mg metal, we will avoid the use of Mg metal in full cells. Then, the changes in the voltage of nano-Sn/MgMn₂O₄ full cell were monitored by using two electrode cells and Mg(ClO₄)₂ in AN as the electrolyte. Several mass ratios *m*₊/*m*₋ were examined.

Figure 7 shows the best response observed that corresponds to a spinel mass excess ($m_+/m_- = 4.0$) that could provide enough magnesium extraction from the cathode during charge to complete Equation (2) in the anode, even if $x = 1.0$. The capacities were thus calculated by using the anode mass. The full Mg-ion cell showed the typical S-shaped voltage profile with an average discharge potential close to 0.8 V and moderate polarization and an increasing discharge capacity up to ca. 150 mA h g^{-1} (Figure 7). This trend is related with the conditioning behavior of the anode that was discussed in the light of Figure 3. An energy density of up to ca. 120 W h kg^{-1} can be estimated considering the mass of the anode.

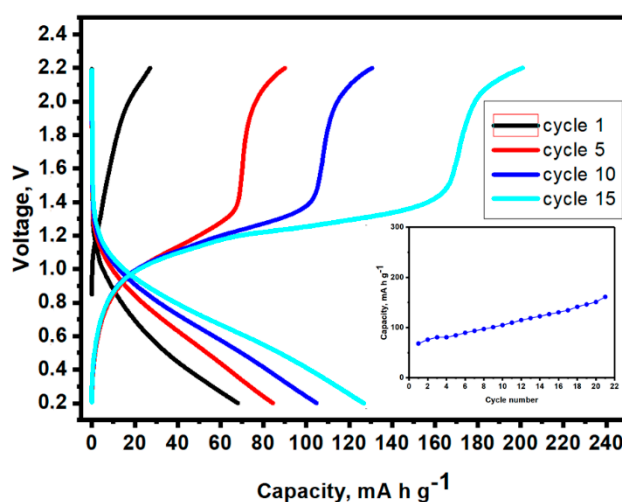


Figure 7. Galvanostatic charge-discharge plot at 20 mA g^{-1} of a nano-Sn/MgMn₂O₄ full cell, using $0.5 \text{ M Mg(ClO}_4)_2$ in AN electrolyte and $m_+/m_- = 4:1$. Inset: Capacity vs. cycle number.

4. Conclusions

The alternative intermetallic anode Mg₂Sn/Sn for Mg-ion batteries is evaluated in Mg half cells with the valuable help of ¹¹⁹Sn Mössbauer spectroscopy. This technique suggests the electrochemical alloying-dealloying properties by a complex mechanism involving amorphous intermetallic phases with an electric field gradient in the environment of tin atoms. The small but significant quadrupolar splitting revealed by the fitting of the spectra of the signal ascribable to the tin-rich phase is indicative of an electric field gradient environment of tin atoms. This is probably due to the presence of lower symmetry environments than in c-Mg₂Sn, because of an incomplete magnesiation. Thus, the coordination polyhedra of tin in c-Mg₂Sn (CaF₂-related structure) are SnMg₈ cubes. For a non-stoichiometric intermediate, SnMg_{8-x} polyhedral are less regular and cause the splitting of the nuclear spin levels of the quadrupolar ¹¹⁹Sn nuclei. Nanoparticulate tin was also examined. Tin nanoparticles are surrounded by a SnO/SnO₂ film due to surface oxidation and are partially reduced during cycling. Their lower diffusion lengths for magnesium improve the initial capacity as compared to tin microparticles, although capacity fading is observed, probably because of the magnesium metal electrodes. Thus, the use of full Mg-ion cells has been tested as a proof of concept. The spinel-related solid, MgMn₂O₄, which is known to deintercalate magnesium by chemical and electrochemical means in both aqueous and non-aqueous electrolytes, was found to be compatible with Mg₂Sn anodes. Cycling properties of the full Mg-ion cells provided voltages around 0.8 V. Capacity values and their retention during cycling were good for the Mg(ClO₄)₂-AN electrolyte. In this case, a reversible discharge capacity of ca. 25 mA h g^{-1} and maximum energy density of ca. 120 W h kg^{-1} were observed.

Author Contributions: All authors contributed substantially to the work reported. Formal analysis, F.N., M.C. and R.A.; Investigation, F.N., M.C., C.P.-V., P.L. and G.F.O.; Project administration, G.F.O. and J.L.T.; Software,

C.P.-V.; Supervision, P.L.; Writing, original draft, R.A., G.F.O. and J.L.T.; Writing, review & editing, P.L., G.F.O. and J.L.T.

Funding: This research was funded by Ministerio de Ciencia, Innovación y Universidades grant numbers MAT2014–56470-R, and MAT2017-84002-C2-1-R), and ERDF funds and Junta de Andalucía grant number FQM288.

Acknowledgments: We also thank the Fine Chemistry Institute (IUIQFN).

Conflicts of Interest: The authors declare no conflict of interest. The funders had no role in the design of the study; in the collection, analyses, or interpretation of data; in the writing of the manuscript, and in the decision to publish the results.

References

1. Gerst, M.D.; Graedel, T.E. In-Use Stocks of Metals: Status and Implications. *Environ. Sci. Technol.* **2008**, *42*, 7038–7044. [[CrossRef](#)] [[PubMed](#)]
2. Tarascon, J.M. Is lithium the new gold? *Nat. Chem.* **2010**, *2*, 510. [[CrossRef](#)] [[PubMed](#)]
3. Wadia, C.; Albertus, P.; Srinivasan, V. Resource constraints on the battery energy storage potential for grid and transportation applications. *J. Power Sources* **2011**, *196*, 1593–1598. [[CrossRef](#)]
4. Speirs, J.; Contestabile, M.; Houari, Y.; Gross, R. The future of lithium availability for electric vehicle batteries. *Renew. Sustain. Energy Rev.* **2014**, *35*, 183–193. [[CrossRef](#)]
5. Lyon, R.E.; Walters, R.N. Energetics of lithium ion battery failure. *J. Hazard. Mater.* **2016**, *318*, 164–172. [[CrossRef](#)] [[PubMed](#)]
6. Novák, P.; Imhof, R.; Haas, O. Magnesium insertion electrodes for rechargeable nonaqueous batteries—A competitive alternative to lithium? *Electrochim. Acta* **1999**, *45*, 351–367. [[CrossRef](#)]
7. Aurbach, D.; Lu, Z.; Schechter, A.; Gofer, Y.; Gizbar, H.; Turgeman, R.; Cohen, Y.; Moshkovich, M.; Levi, E. Prototype systems for rechargeable magnesium batteries. *Nature* **2000**, *407*, 724–727. [[CrossRef](#)] [[PubMed](#)]
8. Saha, P.; Datta, M.K.; Velikokhatnyi, O.I.; Manivannan, A.; Alman, D.; Kumta, P.N. Rechargeable magnesium battery: Current status and key challenges for the future. *Prog. Mater. Sci.* **2014**, *66*, 1–86. [[CrossRef](#)]
9. Zhao-Karger, Z.; Zhao, X.Y.; Wang, D.; Thomas, D.; Behm, R.J.; Fichtner, M. Performance Improvement of Magnesium Sulfur Batteries with Modified Non-Nucleophilic Electrolytes. *Adv. Energy Mater.* **2015**, *5*, 1401155. [[CrossRef](#)]
10. Song, J.; Sahadeo, E.; Noked, M.; Lee, S.B. Mapping the Challenges of Magnesium Battery. *J. Phys. Chem. Lett.* **2016**, *7*, 1736–1749. [[CrossRef](#)] [[PubMed](#)]
11. Jia, X.; Wang, C.; Ranganathan, V.; Napier, B.; Yu, C.; Chao, Y.; Forsyth, M.; Omenetto, F.G.; MacFarlane, D.R.; Wallace, G.G. A Biodegradable Thin-Film Magnesium Primary Battery Using Silk Fibroin–Ionic Liquid Polymer Electrolyte. *ACS Energy Lett.* **2017**, *2*, 831–836. [[CrossRef](#)]
12. Muldoon, J.; Bucur, C.B.; Gregory, T. Quest for Nonaqueous Multivalent Secondary Batteries: Magnesium and Beyond. *Chem. Rev.* **2014**, *114*, 11683–11720. [[CrossRef](#)] [[PubMed](#)]
13. Canepa, P.; Gautam, G.S.; Hannah, D.C.; Malik, R.; Liu, M.; Gallagher, K.G.; Persson, K.A.; Ceder, G. Odyssey of Multivalent Cathode Materials: Open Questions and Future Challenges. *Chem. Rev.* **2017**, *117*, 4287–4341. [[CrossRef](#)] [[PubMed](#)]
14. Okamoto, S.; Ichitsubo, T.; Kawaguchi, T.; Kumagai, Y.; Oba, F.; Yagi, S.; Shimokawa, K.; Goto, N.; Doi, T.; Matsubara, E. Intercalation and Push-Out Process with Spinel-to-Rocksalt Transition on Mg Insertion into Spinel Oxides in Magnesium Batteries. *Adv. Sci.* **2015**, *2*, 1500072. [[CrossRef](#)] [[PubMed](#)]
15. Knight, J.C.; Therese, S.; Manthiram, A. On the Utility of Spinel Oxide Hosts for Magnesium-Ion Batteries. *ACS Appl. Mater. Interfaces* **2015**, *7*, 22953–22961. [[CrossRef](#)] [[PubMed](#)]
16. Cabello, M.; Alcántara, R.; Nacimiento, F.; Ortiz, G.; Lavela, P.; Tirado, J.L. Electrochemical and chemical insertion/deinsertion of magnesium in spinel-type MgMn_2O_4 and $\lambda\text{-MnO}_2$ for both aqueous and non-aqueous magnesium-ion batteries. *CrystEngComm* **2015**, *17*, 8728–8735. [[CrossRef](#)]
17. Singh, N.; Arthur, T.S.; Ling, C.; Matsui, M.; Mizuno, F. A high energy-density tin anode for rechargeable magnesium-ion batteries. *Chem. Commun.* **2013**, *49*, 149–151. [[CrossRef](#)] [[PubMed](#)]
18. Courtney, I.A.; Dunlap, R.A.; Dahn, J.R. In-situ ^{119}Sn Mössbauer effect studies of the reaction of lithium with SnO and $\text{SnO}:0.25 \text{B}_2\text{O}_3:0.25 \text{P}_2\text{O}_5$ glass. *Electrochim. Acta* **1999**, *45*, 51–58. [[CrossRef](#)]

19. Fernández-Madrigal, F.J.; Lavela, P.; Pérez-Vicente, C.; Tirado, J.L.; Jumas, J.C.; Olivier-Fourcade, J. X-ray Diffraction, ⁷Li MAS NMR Spectroscopy, and ¹¹⁹Sn Mössbauer Spectroscopy Study of SnSb-Based Electrode Materials. *Chem. Mater.* **2002**, *14*, 2962–2968. [[CrossRef](#)]
20. Alcántara, R.; Ortiz, G.F.; Lavela, P.; Tirado, J.L. Electrochemical and ¹¹⁹Sn Mössbauer studies of the reaction of Co₂SnO₄ with lithium. *Electrochem. Commun.* **2006**, *8*, 731–736.
21. Aldon, L.; Ionica, C.M.; Lippens, P.E.; Larcher, D.; Tarascon, J.M.; Olivier-Fourcade, J.; Jumas, J.C. In situ ¹¹⁹Sn Mössbauer spectroscopy used to study lithium insertion in c-Mg₂Sn. *Hyperfine Interact.* **2006**, *167*, 729–732. [[CrossRef](#)]
22. Alcántara, R.; Rodríguez, I.; Tirado, J.L. Structural and Electrochemical Properties of Micro- and Nano-Crystalline CoSn Electrode Materials. *ChemPhysChem* **2008**, *9*, 1171–1177. [[CrossRef](#)] [[PubMed](#)]
23. Gogotsi, Y.; Penner, R.M. Energy Storage in Nanomaterials – Capacitive, Pseudocapacitive, or Battery-like? *ACS Nano* **2018**, *12*, 2081–2083. [[CrossRef](#)] [[PubMed](#)]
24. Liu, Z.; Lee, J.; Xiang, G.; Glass, H.F.J.; Keyzer, E.N.; Dutton, S.E.; Grey, C.P. Insights into the Electrochemical Performances of Bi Anodes for Mg-Ion Batteries Using ²⁵Mg Solid State NMR Spectroscopy. *Chem. Commun.* **2018**, *4*, 743–746. [[CrossRef](#)] [[PubMed](#)]
25. Kapitanov, E.V.; Pakovl, E.K. Mössbauer Study of Phase Transitions (I) The Phase Transition of Mg₂Sn. *Phys. State Solids A* **1979**, *53*, 473–480. [[CrossRef](#)]
26. Sirkin, H.; Mingolo, E.; Nassif, N.; Arcondo, B. Increase of the glass-forming composition range of Mg-based binary alloys by addition of tin. *J. Non-Cryst. Solids* **1987**, *93*, 323–330. [[CrossRef](#)]
27. Fries, S.G.; Lukas, H.L. Optimisation of the Mg-Sn System. *J. Chim. Phys.* **1993**, *90*, 181–187. [[CrossRef](#)]
28. Chouvin, J.; Olivier-Fourcade, J.; Jumas, J.C.; Simon, B.; Biensan, P.; Fernández Madrigan, F.J.; Tirado, J.L.; Pérez-Vicente, C. SnO reduction in lithium cells: Study by X-ray absorption, ¹¹⁹Sn Mössbauer spectroscopy and X-ray diffraction. *J. Electroanal. Chem.* **2000**, *494*, 136–146. [[CrossRef](#)]
29. Stockler, H.A.; Sano, H. Mössbauer recoilless fraction in tin compounds. *Nucl. Instrum. Meth.* **1966**, *44*, 103–108. [[CrossRef](#)]



© 2018 by the authors. Licensee MDPI, Basel, Switzerland. This article is an open access article distributed under the terms and conditions of the Creative Commons Attribution (CC BY) license (<http://creativecommons.org/licenses/by/4.0/>).